Supporting information

S doped Fe single atom as efficient peroxidase-like nanozymes for colorimetric detection of oxytetracycline

Jianping Guan [1, #], Tianyu Tao[1, #], Nianhui Zhou[1], Xu Liu[1], Jinhua Hu[1], Chenyang Huang[1], Yunhu Han[2], Tao Gan[3,*], and Yu Xiong[1, *]

AUTHOR ADDRESS

[1] College of Chemistry and Chemical Engineering, Central South University, Changsha 410083, China.

[2] State Key Laboratory of Flexible Electronics, School of Chemistry and Life Sciences, Nanjing University of Posts and Telecommunications, Nanjing, China.

[3] Shanghai Synchrotron Radiation Facility, Shanghai Advanced Research Institute, Chinese Academy of Sciences, Shanghai 201204, China.

[#] These authors contribute equally to the work

* To whom correspondence should be addressed. E-mail: thomas153@126.com, gant@sari.ac.cn

1. Materials and Instruments

1.1 Reagents and materials

Iron acetylacetonate $Fe(acac)_3$, Zinc (II) nitrate hexahydrate ($Zn(NO_3)_2 \cdot 6H_2O$) and 2-methylimidazole (2-MIM), oxytetracycline (OTC) were purchased from Alfa Aesar Chemical Co., Diphenyl disulfide and 3,3',5,5'-tetramethylbenzidine (TMB), Tannic acid (TA), Diphenylditelluride were purchased from Energy Chemical, Levofloxacin, Penicillin, Meropenem, Azithromycin, Enrofloxacin, Ampicillin, Roxithromycin, Fosfomycin, Metronidazole, Cefoxitin, Amoxicillin, Chloramphen, Sulfadiazine, Acetic Acid, Sodium acetate, methanol, isopropanol (IPA) p-benzoquinone (PBQ), and , L-histidine (His) 5,5-Dimethyl-1-pyrrolineN-oxide (DMPO), and ethanol were purchased at the Shanghai Sinopharm Chemical Reagent Co. Shanghai Sinopharm Group Chemical Reagent Company. All chemicals were analytical grade and directly used without further purification. Solutions were prepared with ultrapure water from Millipore Milli-Q water purification system (Billerica, MA).

1.2 Instruments

The particle morphology observation primarily relied on the JEM-F200 scanning transmission electron microscope working at 200 kV. , whose STEM mode provides a resolution better than 0.16 nm. Regarding the detection limit for particle identification, we define it as the minimum particle size that can be reliably recognized and statistically analyzed under specific imaging and analytical conditions. For morphological identification, considering limitations in signal-to-noise ratio and contrast, we set the lower size limit for statistical analysis at 2 nm, which is significantly higher than the theoretical instrumental resolution, to ensure statistical reliability. For compositional identification, the energy-dispersive X-ray spectroscopy (EDS) system used typically has an elemental detection limit in the range of 0.1–0.5 wt.% (depending on the specific element), which ensures the accuracy of the compositional analysis for the particles examined. Aberration corrected high-angle annular dark-field scanning TEM (AC-HAADF STEM) images were taken on a JEM-ARM200F atomic-resolution analytical microscope operated at 300 kV. X-ray diffraction (XRD) patterns were recorded using a Rigaku MiniFlex600 X-ray powder diffractometer with monochromatized Cu Kα radiation (λ = 1.5406 Å). Fe K-edge XAFS measurements of **Fe_1/SCN** were carried out at the 1W1B station in Beijing Synchrotron Radiation Facility (BSRF, 2.5 GeV, 250 mA maximum, Si(111) double crystals monochromator). The XAFS raw data was background-subtracted, normalized and Fourier-transformed by standard procedures with the ATHENA program. Nitrogen adsorption and desorption experiments were carried out on an Autosorb iQ2 adsorptometer (Quantachrome Instruments) at 77 K, and specific surface areas were calculated through Langmuir equation. Pore size distribution was estimated from the adsorption branch of the isotherm by the nonlocal density-functional theory (NLDFT) method. XPS spectra were performed by a Thermo Fisher ESCALAB Scientific ESCALAB 250Xi XPS System. V-vis absorption spectra were recorded with a UV-2600 spectrophotometer (Shimadzu, Japan).

2. Experiment Section

2.1 Synthesis of H-ZIF-8

In a typical synthesis, 1.192 g of $Zn(NO_3)_2 \cdot 6H_2O$ was dissolved in 30 mL of methanol, and the resulting solution was added to 15 mL of methanol containing 1.314 g of 2-methylimidazole. The mixture was stirred at room temperature for 1 hour, transferred to a Telfon-lined stainless-steel autoclave, and maintained at 120°C for 4 hours. After cooling to room temperature, the solid product was collected by centrifugation. The dried solid was then dissolved in methanol, followed by the addition of a 30 g/L tannic acid solution. The mixture was stirred for 50 minutes, after which the solid product was isolated again by centrifugation. Finally, the product was dried overnight in an 80°C vacuum oven to yield the final material.

2.2 Synthesis of CN and SCN

CN was derived from H-ZIF-8 powder via pyrolysis at 950 °C for 3 h under a N_2 atmosphere, employing a heating rate of 5 °C min^{-1}. The SCN material was obtained by annealing a ground mixture of CN (25 mg) and diphenyl disulfide (1 mg) at 950 °C for 2 h under N_2 flow (5 °C min^{-1}).

2.3 Preparation of Fe_1/SCN and Fe_1/CN

The Fe_1/SCN material was obtained by annealing a ground mixture of CN (25 mg), iron acetylacetonate (2 mg), and diphenyl disulfide (1 mg) at 950 °C for 2 h under N_2 flow (5 °C min^{-1}).[1,2] The reference Fe_1/CN material was prepared under identical conditions in the absence of diphenyl disulfide.

2.4 Investigation of Peroxidase-like Activity

The peroxidase-like activity of Fe_1/SCN was systematically evaluated across a range of pH and temperature conditions using H_2O_2 and TMB as chromogenic substrate. To investigate the effect of pH on the catalytic activity of nanoenzymes, the reaction mixture consisted of 1940 μL of 0.2 M acetate buffer (pH 3.0–7.0), 20 μL of 20 mM TMB, 20 μL of 200 mM H_2O_2, and 20 μL of Fe_1/SCN suspension (1 mg/mL). After incubation at 25°C for 5 min in the dark, the absorbance was measured at 652 nm using a UV−visible spectrophotometer.

Building on the identified optimal pH profile, we further examined how temperature modulates the catalytic performance of Fe_1/SCN. Reaction mixtures containing Fe_1/SCN, TMB, H_2O_2, and acetate buffer (pH 4.0) were incubated in the dark across a temperature gradient (10-80°C). The resulting absorbance at 652 nm was used to establish the optimal pH-temperature combination for maximum catalytic efficiency.

A series of control experiments were conducted by varying the concentrations of TMB or H_2O_2 across specified concentration ranges, with all other experimental parameters held constant. The Michaelis constant (K_m) and maximum reaction rate (V_{max}) were determined from the Lineweaver-Burk plot using the transformed Michaelis-Menten equation: $1/V = K_m/V_{max} \times (1/[S] + 1/K_m.)$

2.5 Specific activity calculation

The specific activity (SA) of three catalysts were confirmed by the color change of TMB. Different concentrations of three catalysts were added to the mixed system containing TMB (20 mM), and the final system was adjusted to 1.5 mL.

Calculate the nanozyme activity (units) using the following equation:

$b_{nanozyme} = V/ (\varepsilon \text{ x } 1) \text{ x } (\triangle A/\triangle t)$ (2)

where bnanozyme is the catalytic activity of nanozyme expressed in units. One unit is defined as the amount of nanozyme that catalytically produces 1 μmol of product per min at room temperature; V is the total volume of reaction solution (μL); ε is the molar absorption coefficient of the colorimetric substrate, which is maximized at 39,000 M^{-1} cm^{-1} at 652 nm for TMB; l is the path length of light traveling in the cuvette (cm); A is the absorbance after subtraction of the blank value; and ΔA/Δt is the initial rate of change in absorbance at 652 nm min^{-1}.

Calculate the SA of the Fe_1/CN, and Fe_1/SCN (U mg^{-1}) by

SA= $b_{nanozyme}$/ [m]   (3)

where SA is the specific activity expressed in units per milligram (U mg^{-1}) nanozymes, and [m] is the nanozyme weight (mg) of each assay.

2.6 Colorimetric determination of OTC

Leveraging the peroxidase-like activity of Fe_1/SCN toward the TMB–H_2O_2 system, a colorimetric method was developed for the visual and quantitative detection of oxytetracycline (OTC). All detection procedures were performed under previously optimized catalytic conditions. Specifically, Fe_1/SCN and OTC at varying concentrations (0–30 μM) were mixed with 1930 μL of sodium acetate buffer and incubated for 10 min at room temperature. Then, 20 μL of H_2O_2 and 20 μL of TMB solution were sequentially introduced into the mixture. After 5 min of reaction in the dark, the absorbance at 652 nm was recorded.

Based on the experimental results, we observed a progressive fading of the blue coloration with increasing oxytetracycline (OTC) concentration, demonstrating that OTC effectively suppresses the catalytic activity of Fe_1/SCN. The degree of suppression is positively correlated with the OTC concentration. We quantified this inhibitory effect by measuring absorbance changes using UV-vis spectroscopy. The establishment of a linear calibration curve relating absorbance variation to OTC concentration enabled determination of the limit of detection (LOD), thereby achieving sensitive quantification of OTC.

2.7 Anti-Interference and selectivity experiment

To evaluate the selectivity of the Fe_1/SCN/TMB–H_2O_2 system for OTC detection, the following experiment was conducted: identical concentrations (10 μM) of OTC and

13 other antibiotics (Levofloxacin, Penicillin, Meropenem, Azithromycin, Enrofloxacin, Ampicillin, Roxithromycin, Fosfomycin, Metronidazole, Cefoxitin, Amoxicillin, Chloramphen, Sulfadiazine) were separately mixed with 20 μL of Fe_1/SCN (1 mg/mL) in 1930 μL of sodium acetate buffer (200 mM, pH = 4) and incubated at room temperature for 10 min. Subsequently, 20 μL of H_2O_2 (200 mM) and 20 μL of TMB (20 mM) solution were added sequentially, resulting in a total reaction volume of 2 mL. After reacting in the dark for 5 min, the absorbance at 652 nm were determined.

To investigate the potential interference effects of coexisting substances on OTC detection, 20 μM of each of the other 13 antibiotics was individually added to a 10-μM OTC solution. Subsequently, 20 μL of Fe_1/SCN (1 mg/mL) was introduced into the mixture, followed by the addition of 1930 μL of sodium acetate buffer (200 mM, pH = 4). After incubating at room temperature for 10 minutes, subsequent operations were carried out according to the method described above, and finally, the absorbance of the reaction system at 652 nm was measured.

2.8 Mechanism study

Free radical scavenging experiment: Fe_1/SCN (20 μL, 1.0 mg mL^{-1}), p-benzoquinone (100 μL, 10 mM) and TMB (30 μL 20 mM) were mixed with HAc-NaAc buffer solution (1850 μL 0.2 M, pH=4.0). After incubation at room temperature for 10min, the absorbance of the system at 652 nm was measured. Subsequently, p-benzoquinone was replaced with tryptophan (5 mM), and isopropanol (5 mM) in sequence, and the absorbance of the system in the presence of different free radical scavengers was recorded.

The mechanistic influence of oxytetracycline (OTC) on the Fe_1/SCN-catalyzed TMB-H_2O_2 colorimetric system was investigated using electron paramagnetic resonance (EPR). Specifically, DMPO was employed as $•O_2^-$ scavenger to probe the reaction pathway. In these experiments, the Fe1/SCN-H_2O_2-TMB system was supplemented with 50.0 μL of DPMO solution, 50 μL of OTC (1 mg/mL), or both agents simultaneously. After a 5-minute incubation period, Subsequently, EPR spectra were acquired to directly monitor the effect of OTC on the evolution of radical species during the reaction.

2.9 Detection of OTC in Actual Samples

The detection capability of the Fe_1/SCN-based colorimetric sensing platform for real-sample analysis was evaluated through standard addition recovery experiments using three environmentally relevant water matrices: Xiangya Medical Wastewater, Aviation honey, and Raw milk. Prior to analysis, all water samples were pre-filtered through 0.2 μm microporous membranes to eliminate suspended particulates and interfering impurities. Oxytetracycline standard solutions at three concentrations (0.6, 9.0, and 27.0 μM) were introduced into the pretreated environmental water samples. The absorbance of each spiked sample was measured by UV-visible spectrophotometry, and the corresponding OTC concentrations were quantified against a pre-established calibration curve. Recovery rates were calculated according to the formula: Recovery (%) = (measured concentration/spiked concentration) × 100. These recovery data validate the accuracy and reliability of the method in complex aqueous matrices.

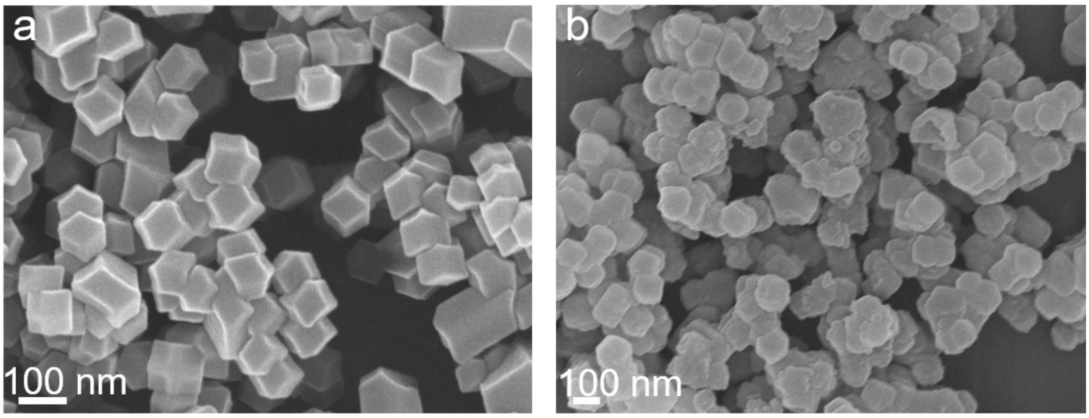

Figure S1: SEM image of ZIF-8(a) and H-ZIF-8 (b).

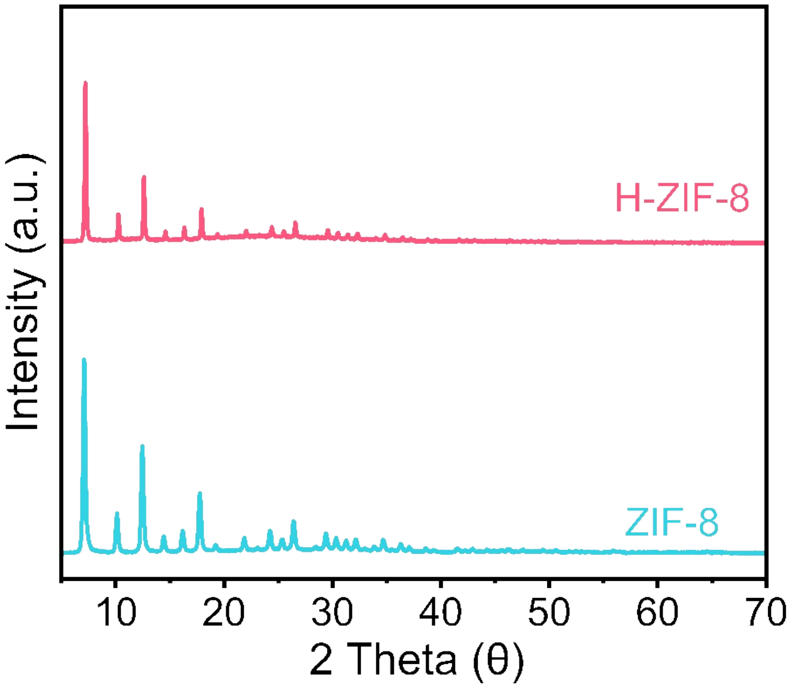

Figure S2: XRD patterns of H-ZIF-8 and ZIF-8.

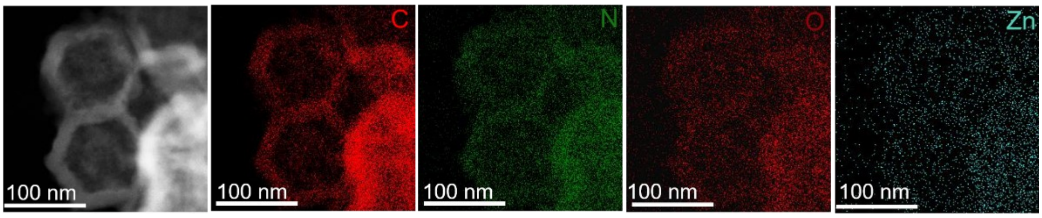

Figure S3. STEM image and the corresponding EDS mapping images of CN.

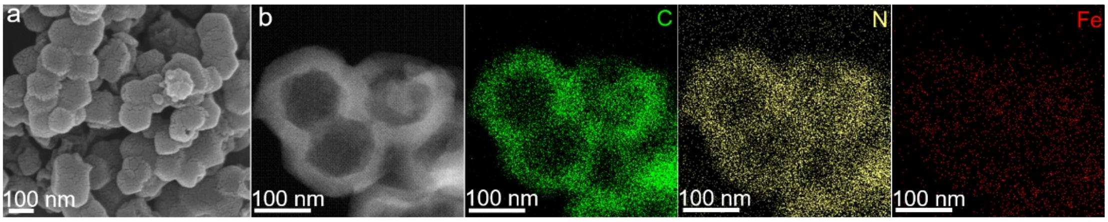

Figure S4. (a) SEM image and (b) STEM image and the corresponding EDS mapping images of Fe$_1$/CN.

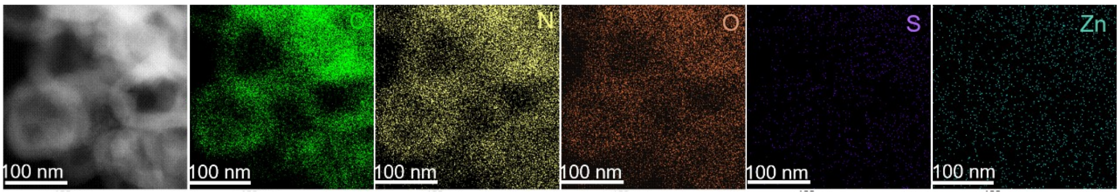

Figure S5. STEM image and the corresponding EDS mapping images of SCN.

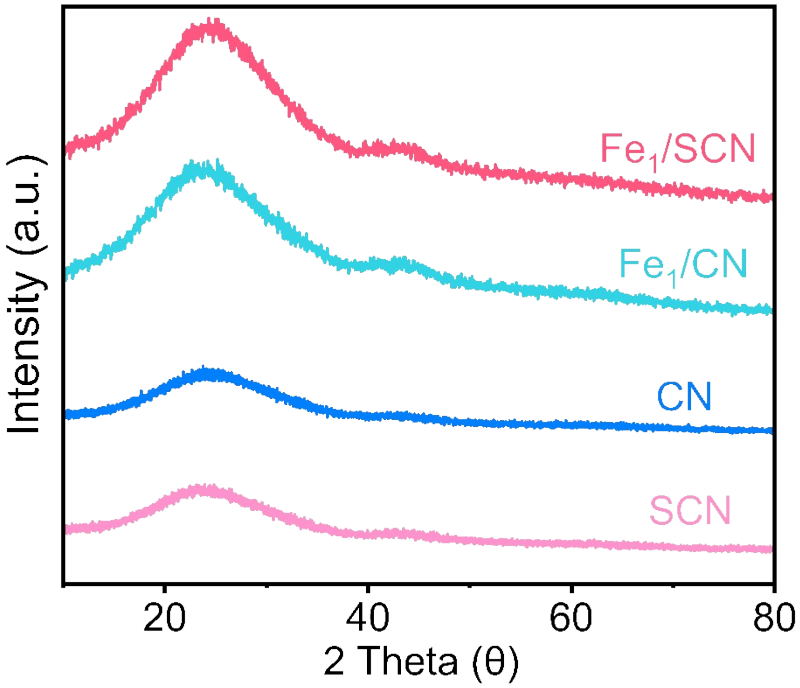

Figure S6. XRD patterns of Fe$_1$/CN, Fe$_1$/SCN, SCN, and CN.

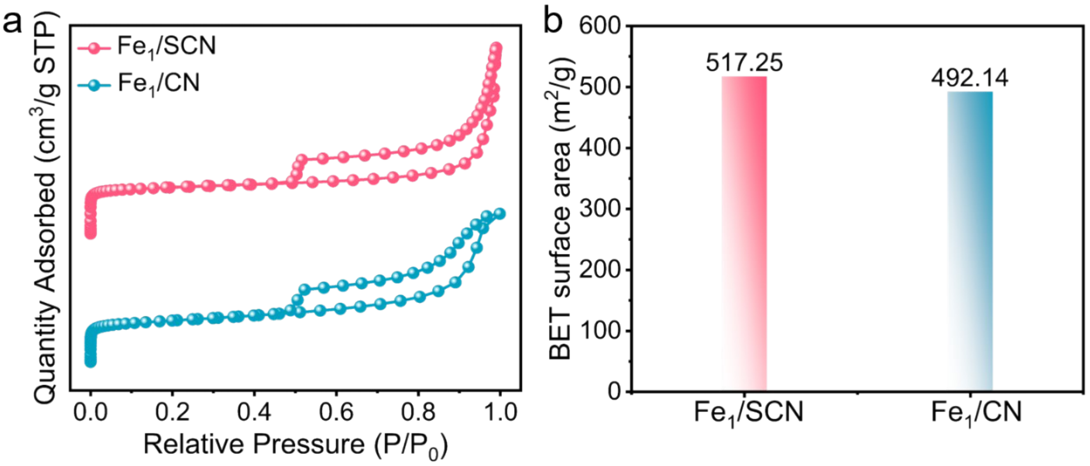

Figure S7. N_2 adsorption/desorption isotherms (a) and BET surface areas (b) of Fe$_1$/SCN, an Fe$_1$/CN.

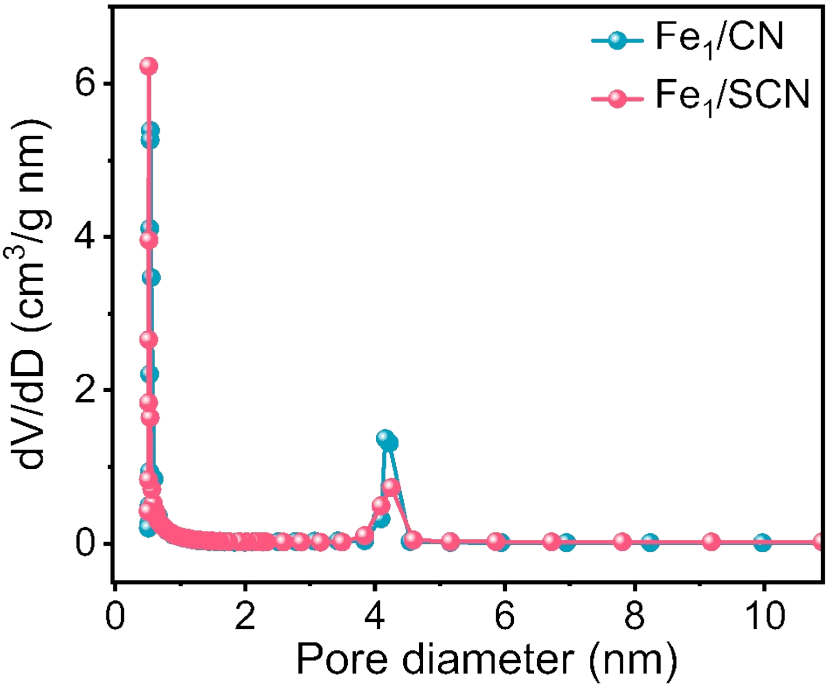

Figure S8. Pore diameter distribution for Fe$_1$/SCN, and Fe$_1$/CN catalysts.

Table S1. The BET surface area, pore diameter and pore volume of Fe_1/SCN, and Fe_1/CN catalysts.

Samples	BET surface area (m^2 g^{-1})	Pore diameter (nm)	Microporous diameter (nm)	Mesoporous diameter (nm)	Pore volume (cm^3 g^{-1})
Fe_1/CN	492.14	3.33	0.51	3.50	0.81
Fe_1/SCN	517.25	3.96	0.54	5.12	1.02

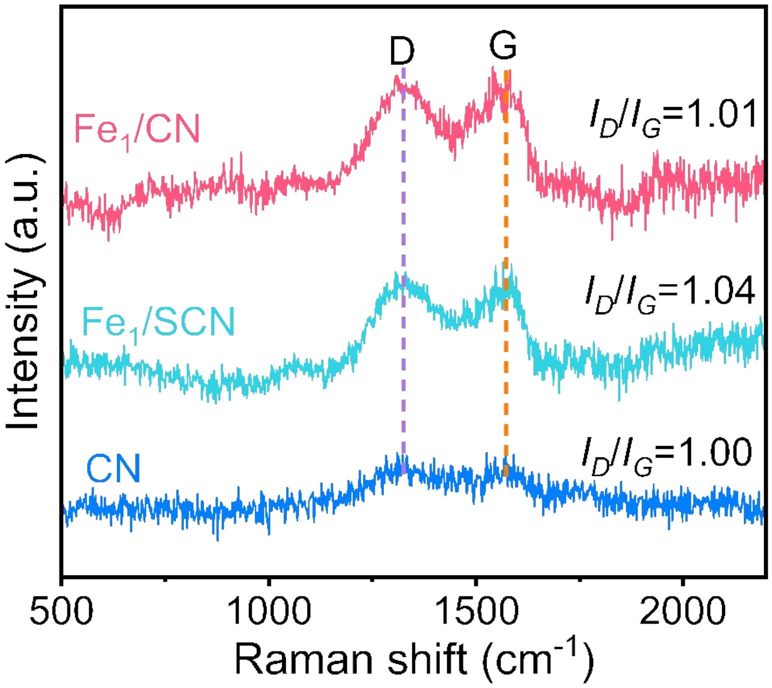

Figure S9. Raman spectra of CN, Fe_1/SCN, and Fe_1/CN catalysts.

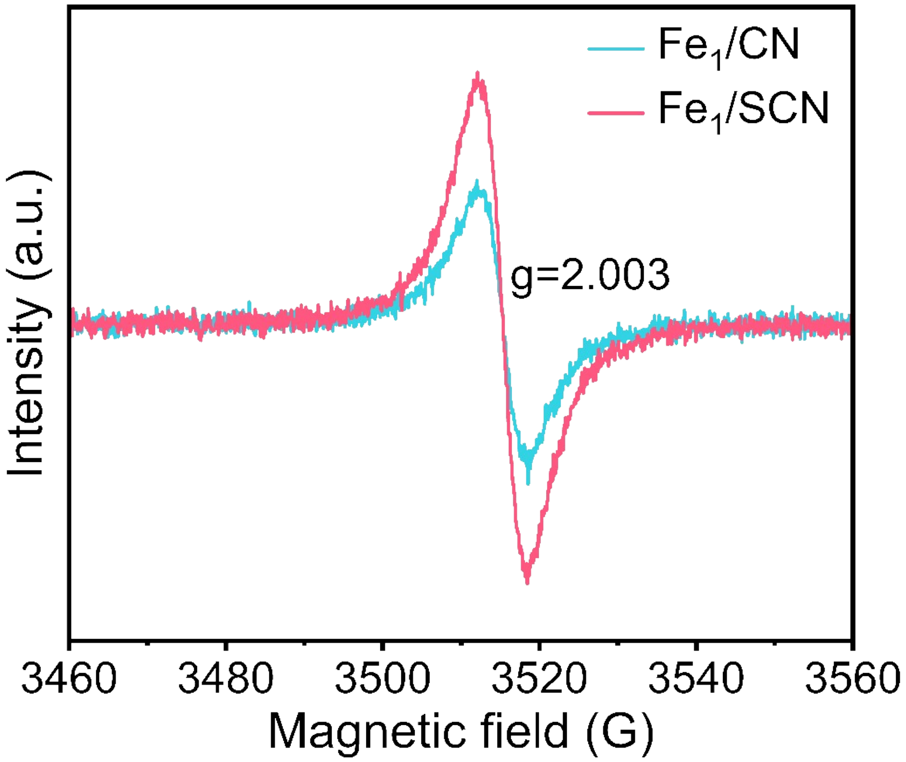

Figure S10. EPR spectra of Fe$_1$/CN.and Fe$_1$/SCN.

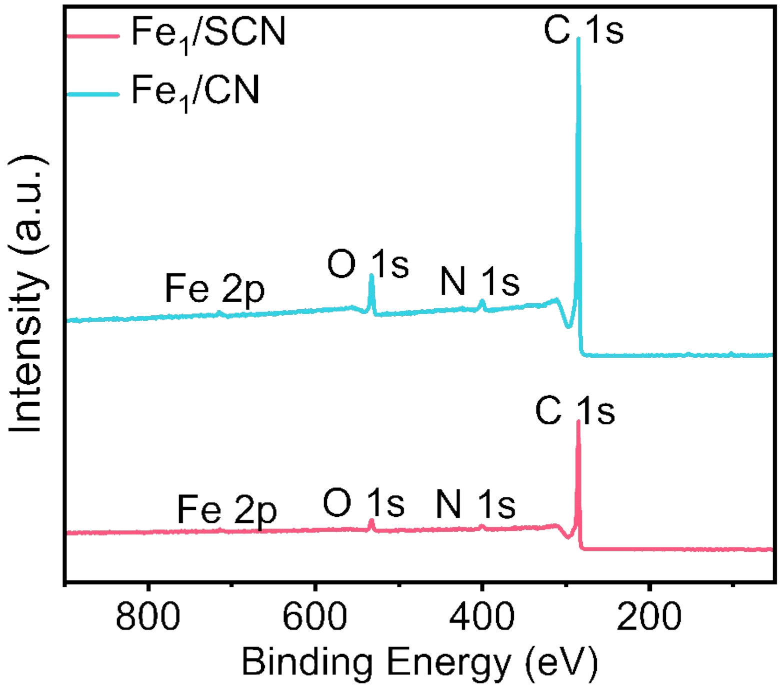

Figure S11. XPS surveys of Fe_1/SCN, and Fe_1/CN.

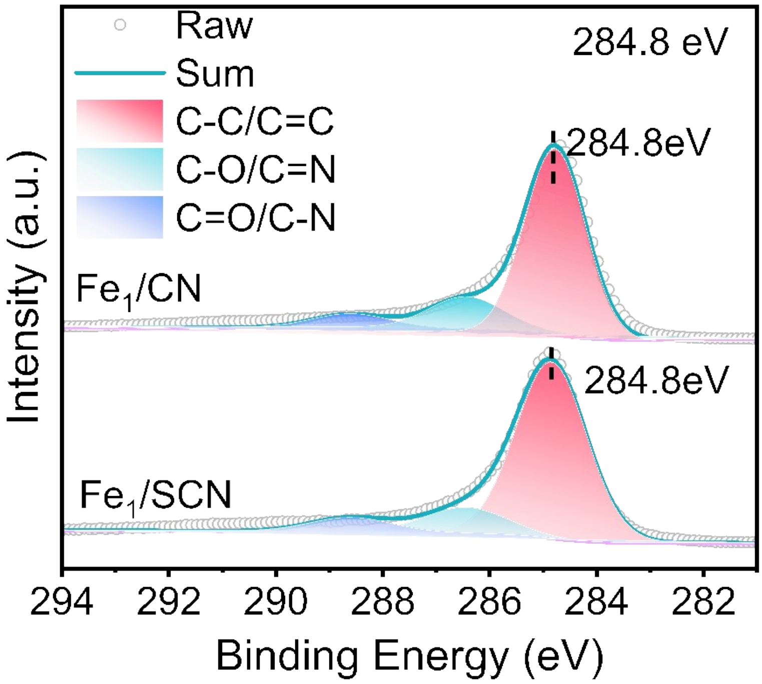

Figure S12. XPS spectra of C 1s for Fe_1/SCN, and Fe_1/CN catalysts.

Table S2. The statistical results of C, N, S and Fe atomic percentage from XPS.

Peak Table		
Name	**FWHM eV**	**Atomic %**
C1s	1.47	94.95
N1s	2.62	4.04
S2p	1.49	0.6
Fe2p	0.16	0.41

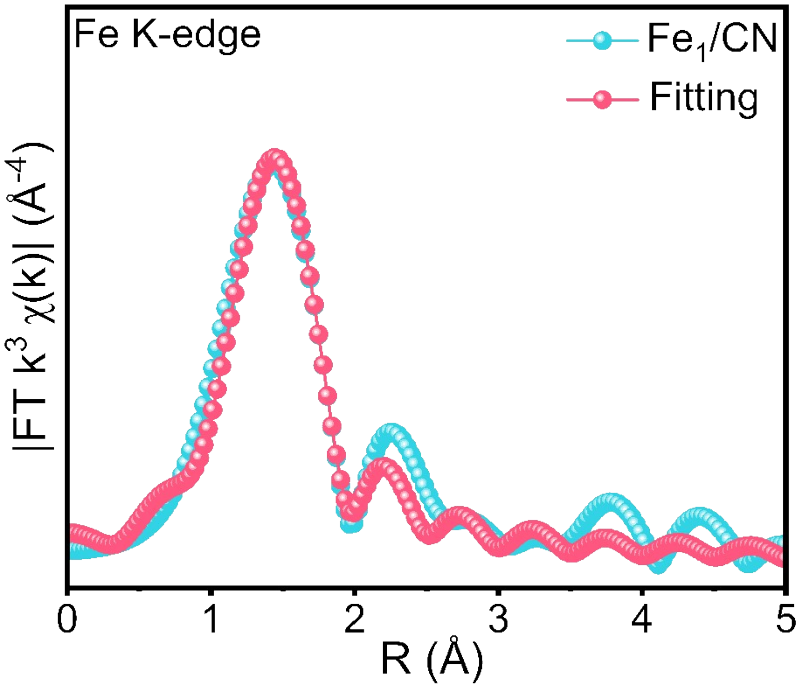

Figure S13. EXAFS fitting curves at the R space of Fe_1/CN.

Table S3. Fitting Parameters of Fe K-edge EXAFS curve.

Sample	**Shell**	**CN**	**R(Å)**	**σ^2(Å^2)**	**ΔE_0(eV)**	**R factor**
Fe_1/CN	Fe-N	4.42	1.99	0.006	1.59	0.019
Fe_1/SCN	Fe-N	4.41	2.00	0.006	0.93	0.011

CN was coordination numbers. R was bond distance. $\sigma^2$was Debye-Waller factors. ΔE_0 was the inner potential correction. R factor reflected goodness of fitting. S_0^2 was set to 0.87, according to the experimental EXAFS fitting of Te foil by fixing CN as the known crystallographic value. Error bounds were estimated as CN ± 20%; R ± 1%; σ^2 ± 20%.

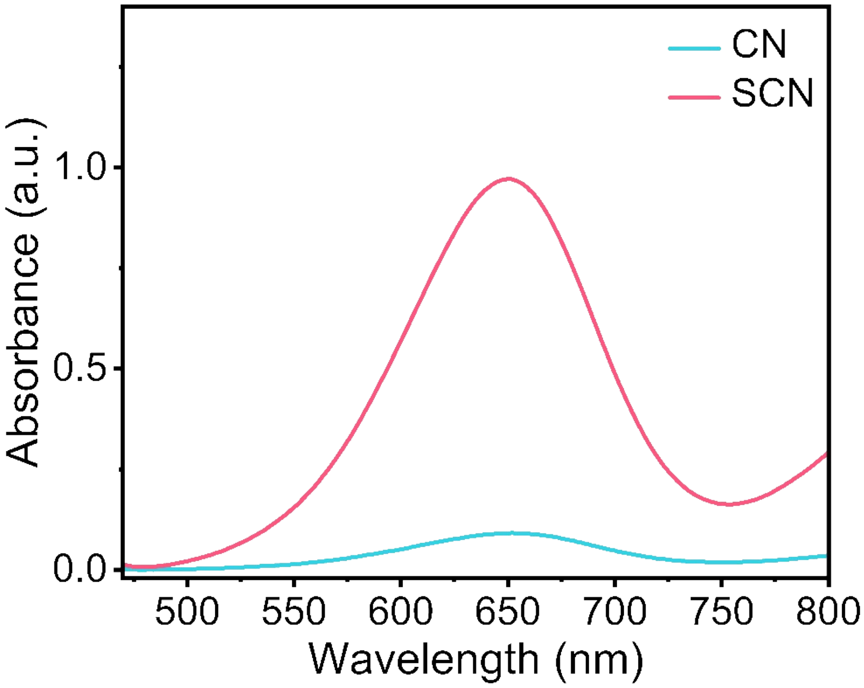

Figure S14. UV-vis absorption spectra of SCN and CN reaction with H_2O_2+TMB.

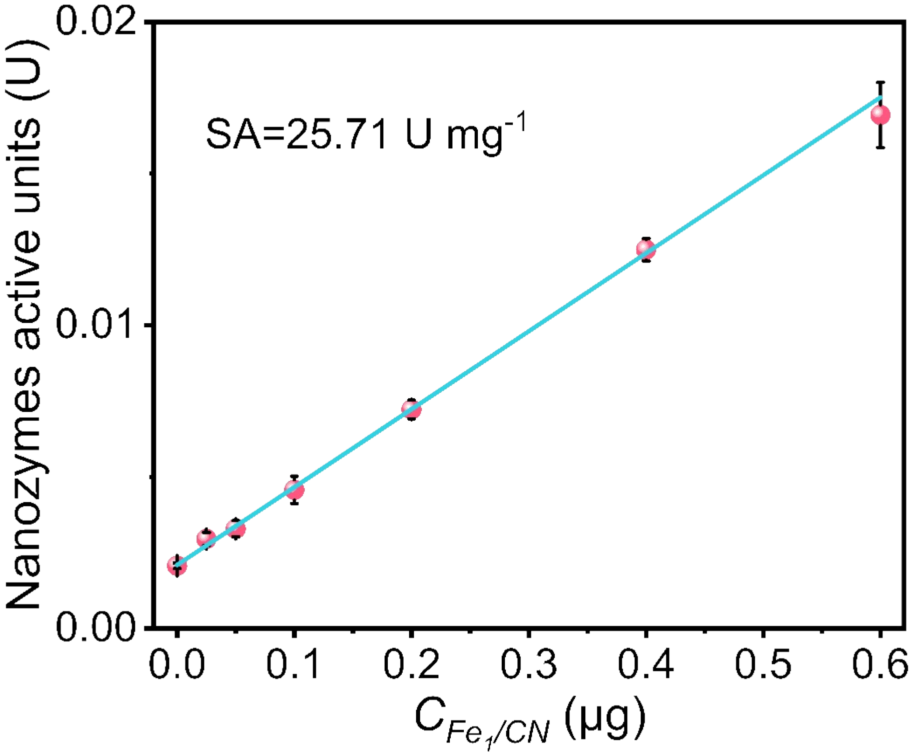

Figure S15. Specific activity analysis of Fe_1/CN catalysts.

Table S4. Comparison of the specific activity of Fe_1/SCN and Fe_1/CN with other materials

SAzymes	**POD-like specific activity (U mg^{-1})**	**Ref.**
Fe_1/SCN	89.08	This work
Fe_1/CN	25.71	This work
MnSA-N_3-C	51.3	[3]
Cu-JMCNs	2.46	[4]
FeN_5–SA	30.96	[5]
CuN_3	11.33	[6]
Pt_{TS}	21.8	[7]
FeNCP/NWs	86.9	[8]
FeNC/NW	47.1	[8]
FeCuNC	33.87	[9]
FeNC	3.54	[9]
FeNC/NW	47.1	[10]
FeBNC	15.41	[10]
FeNC	4.09	[10]
H-MoN_5@PtN_4/C	34.33	[11]
Fe─B/N─C	103.82	[12]
Fe-N-C SAzymes	36.93	[12]
Zn-SA/CNC	66.7	[13]
Fe-SASC/NW	42.8	[14]
FeNC	24.83	[15]
FeSNC	79.71	[15]
GOD@FeN_4-SAzyme	60.57	[16]
FeSA	19.3	[17]
FeSA-PtC	87.7	[17]
Fe-N_5/SAC	71.99	[18]
FeN_4	25.33	[19]
FeN4-SAzyme	33.8	[20]
Fe_3C@C/Fe-N-C	23.01	[21]
Fe-N-C	10.12	[21]
NG-Heme	67.3	[22]
Mn/PSAE	5.04	[23]

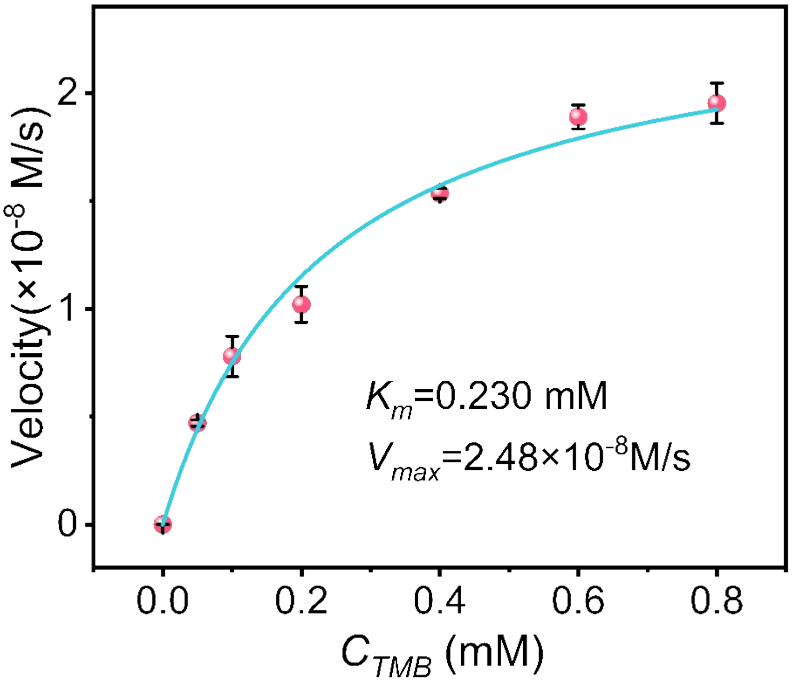

Figure S16. Steady-state kinetic assay of Fe_1/CN with TMB as substrate.

Table S5. Kinetics parameters comparison of the Fe_1/SCN and Fe_1/CN with other catalysts

Catalyst	**[E] (M)**	***Km* (mM)**	***Vmax* *(10^{-8} M s^{-1})***	***V_{max}/m***	***kcat* *(s^{-1})***	***kcat*/*Km* (mM^{-1} s^{-1})**	**Ref.**
FeNSC	8.495×10^{-9}	0.067	4.70	47	5.53	81.34	This work
FeNC	8.495×10^{-9}	0.23	2.48	24.8	2.91	12.68	
CuN_3-SAzyme	9.31×10^{-6}	1.61	164	45.56	0.18	109.3	[4]
Fe—B/N—C	2.03×10^{-7}	0.378	357.5	71.5	17.61	46.6	[10]
f-FeNC	8.06×10^{-8}	0.154	3.61	7.22	0.45	2.92	[22]
Fe-S/N-C	2.6×10^{-7}	0.33	130	74.28	5.02	15.21	[23]
Fe SAEs	1.07×10^{-6}	3.92	58.8	58.8	0.55	0.14	[24]
Cu-N-C	2.68×10^{-6}	3.76	75.05	75.05	0.283	0.0746	[25]
Fe-MOF	4.9×10^{-5}	2.6	5.6	0.56	0.0011	0.42	[26]
Cu–N–C	2.68×10^{-6}	3.76	75.1	75.1	0.28	0.075	[27]
Zn-N-C	4.8×10^{-5}	0.224	10.66	10.66	0.0022	9.8	[28]
Fe_3O_4	3.87×10^{-3}	0.382	123	4.1	3.18×10^{-5}	8.32×10^{-5}	[29]
Fe SAEs	1.07×10^{-6}	3.92	58.8	58.8	/	/	[30]
G-Heme	2.67×10^{-6}	0.35	0.27	0.3	0.010	29.14	[20]
Fe-N-C	7.48×10^{-6}	1.48	5.6	0.56	0.075	50.67	[8]
Cu-N-C	2.68×10^{-6}	3.76	20.1	20.1	0.2803	74.6	[31]
Cu NPs/N-C	2.58×10^{-5}	1.57	12.76	12.76	0.0049	3.1	[31]

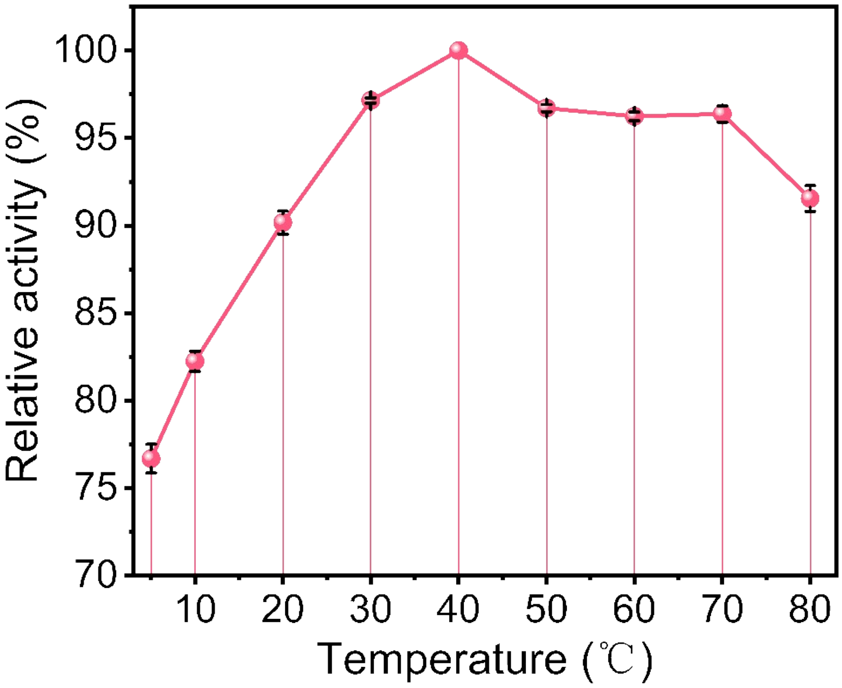

Figure S17. Relative activity of Fe_1/SCN reaction system for POD-like activity under different temperature (5–80°C).

.

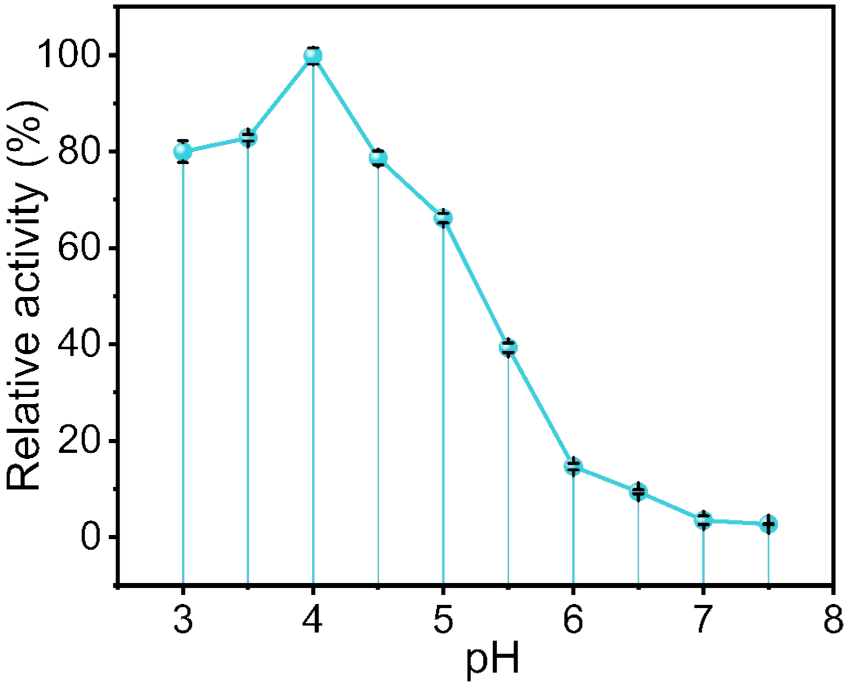

Figure S18. Relative activity of Fe_1/SCN reaction system for oxidase-like activity within pH range (3.0–7.5).

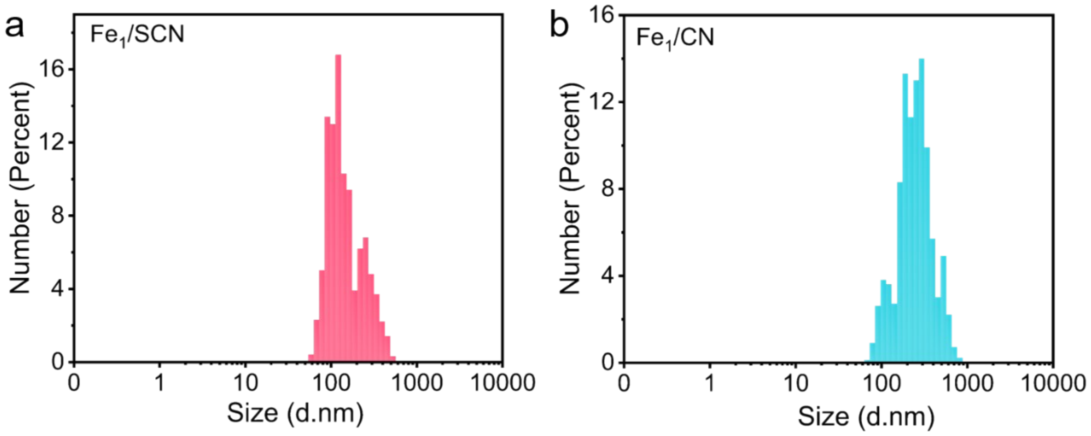

Figure S19. The dynamic light scattering (DLS) particle size analysis on Fe_1/SCN (a) and Fe_1/CN (b) in buffer solution.

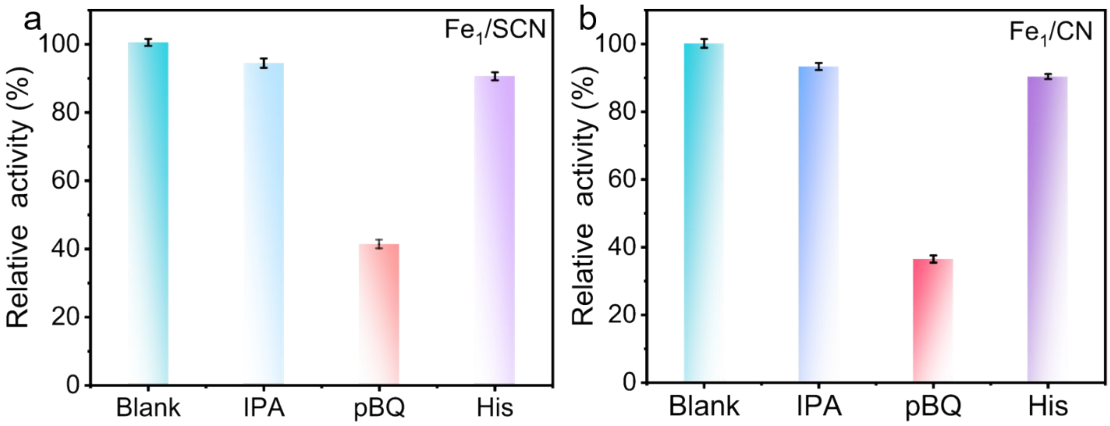

Figure S20. Effect of free radical scavengers on the performance of Fe_1/SCN (a) and Fe_1/CN (b).

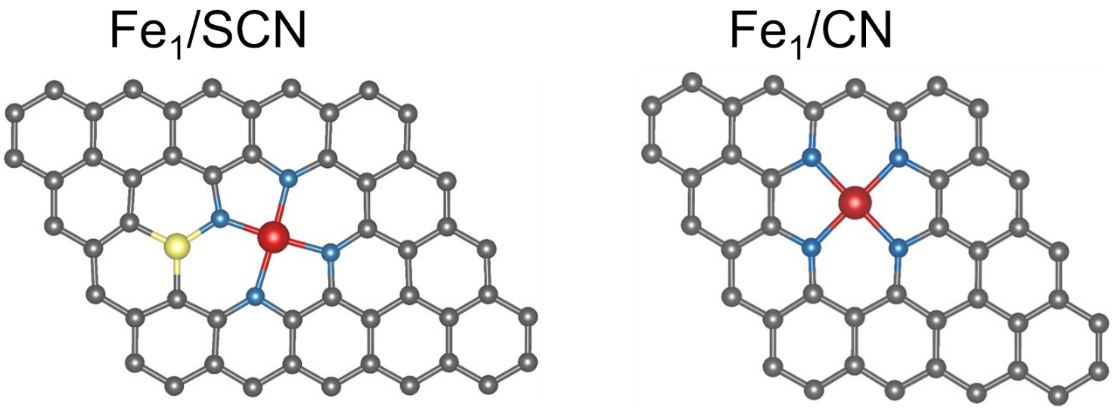

Figure S21. Structural model optimization of Fe_1/SCN and Fe_1/CN.

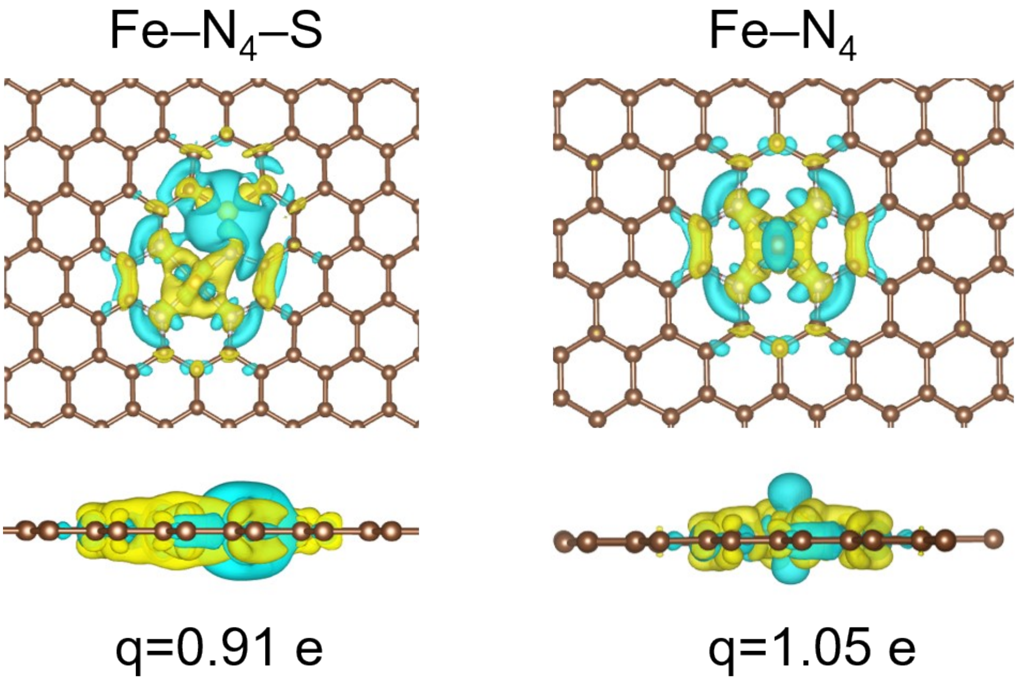

Figure S22. The charge density difference and Bader charge of Fe-N$_4$ and (b) Fe-N$_4$-S.

Bader charge analysis reveals that the Fe atom carries charges of +1.05 e and +0.91 e in the Fe–N$_4$ and Fe–N$_4$–S configurations, respectively, indicating that S-doping in the second coordination shell effectively modulates the electronic structure of the Fe center, resulting in a lower oxidation state of Fe in Fe–N$_4$–S compared to the planar Fe–N$_4$ site. The electron localization between Fe–S and Fe–N bonds (green regions between Fe–S and Fe–N bonds) is lower than that in Fe–N bonds, which is attributed to the weaker electron-withdrawing effect of S. This distinct electronic environment induces charge polarization, thereby optimizing the adsorption–desorption behavior of oxygen intermediates and leading to significantly enhanced catalytic activity.

Scheme S1. The POD-like reaction pathways involve four elementary steps

$$\text{(I) } H_2O_2 \rightarrow {*}\,H_2O_2$$

$$\text{(II) } {*}\,H_2O_2 + H^{+} + e^{-} \rightarrow {*}OH + H_2O$$

$$\text{(III) } {*}OH + H_2O_2 \rightarrow \bullet OOH + {*}\,H_2O$$

$$\text{(IV) } {*}\,H_2O \rightarrow {*} + H_2O$$

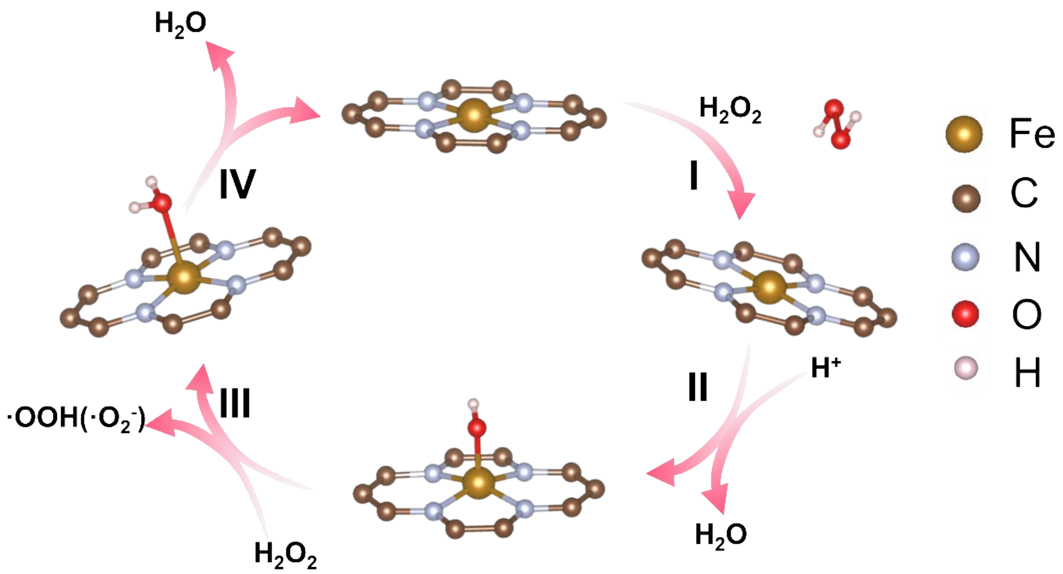

Figure S23. Schematics of the proposed reaction pathways of Fe_1/CN for POD-like reaction.

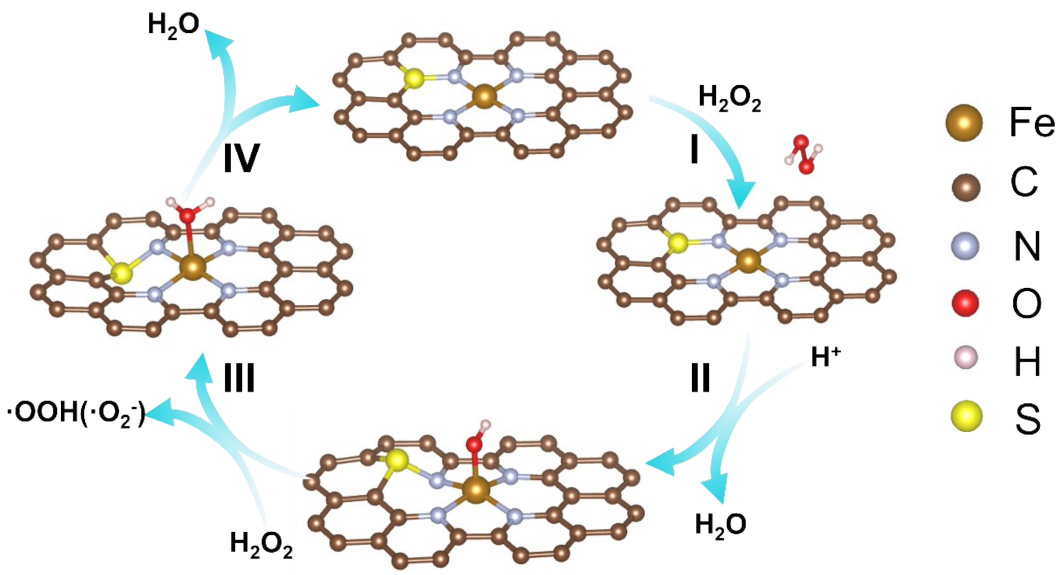

Figure S24. Schematics of the proposed reaction pathways of Fe$_1$/SCN for POD-like reaction.

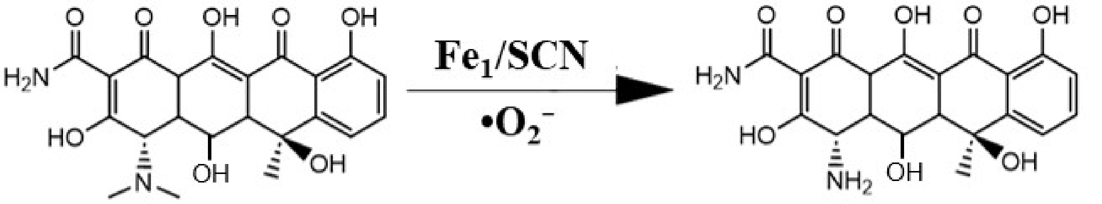

Figure S25. The possible pathway for the consumption of $\bullet O_2^-$ by OTC in the Fe_1/SCN-catalyzed TMB-H_2O_2 system.

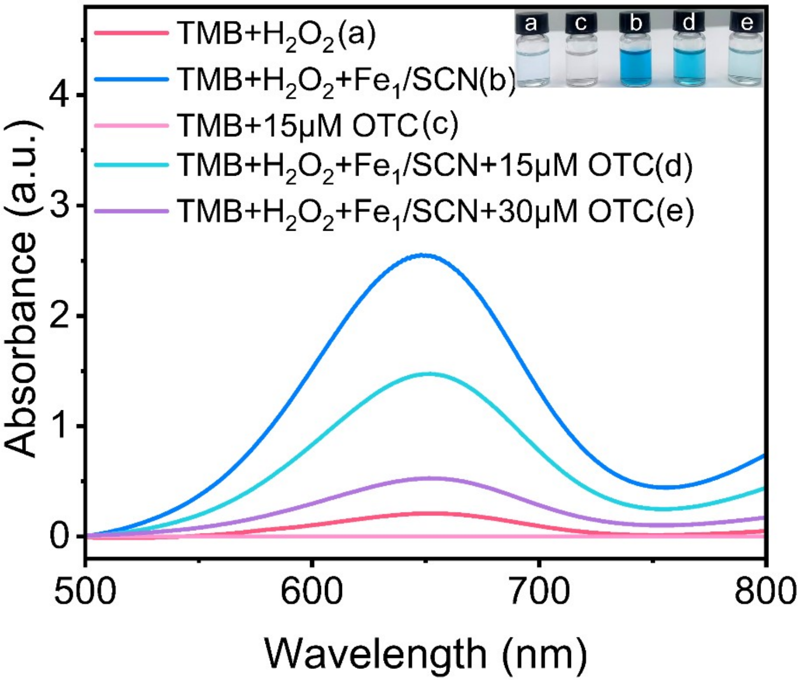

Figure S26. UV–vis spectra of Fe_1/SCN+ TMB+H_2O_2, Fe_1/SCN+ OTC + TMB+H_2O_2, TMB+H_2O_2, and OTC + TMB.

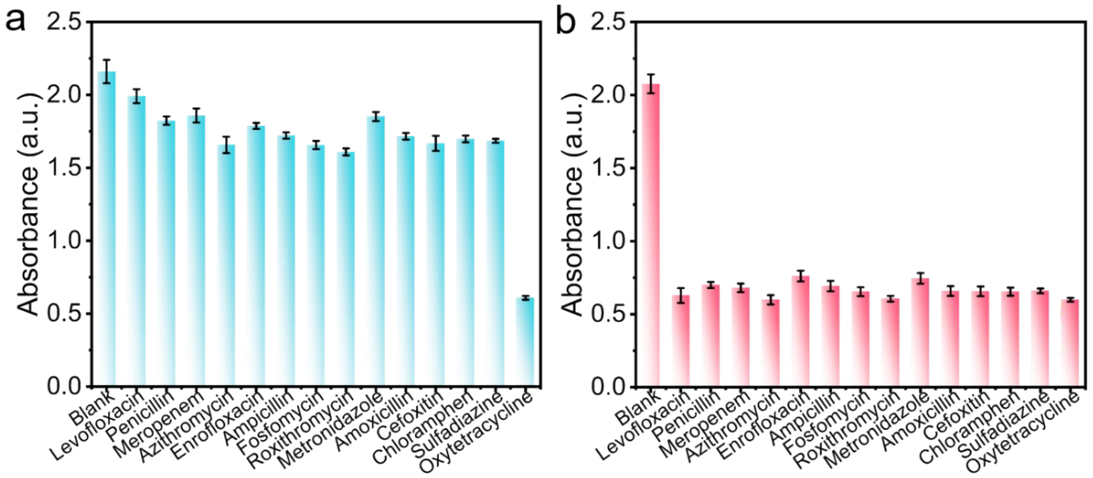

Figure S27. (a) The selectivity of the OTC detection for Fe_1/SCN+TMB+H_2O_2 system. (b) Anti-interference ability of Fe_1/SCN+TMB+H_2O_2 by mixing OTC with other interferents (Fe_1/SCN: 1 mg/mL; H_2O_2: 200 mM; TMB: 20 mM; OTC: 10 µM, other 13 antibiotics: 20 µM; sodium acetate buffer: 200 mM, pH = 4).

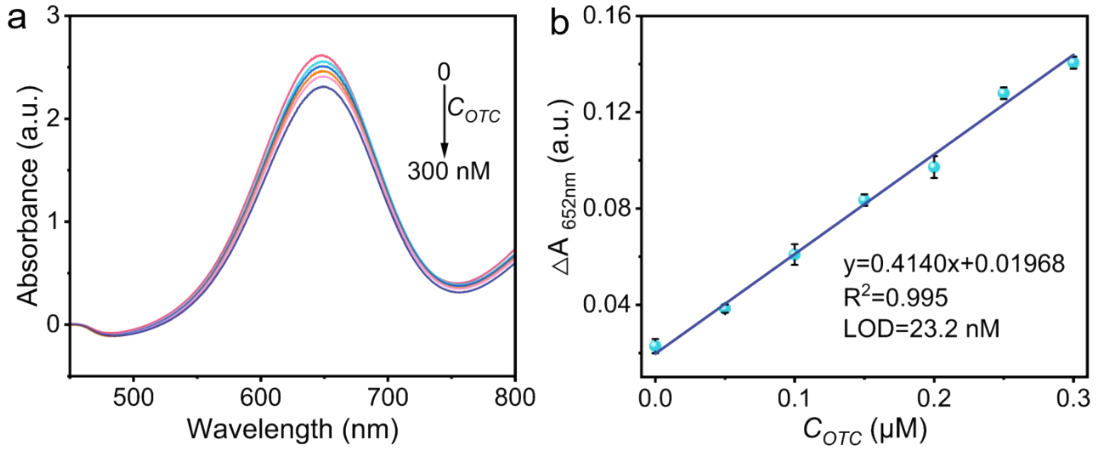

Figure S28. (a) UV-vis absorption spectra of Fe_1/SCN+TMB+H_2O_2 with different OTC concentrations (0-300 nM). (b) Relationship between the absorbance change ($\Delta A_{652\ nm}$) and the concentration of OTC.

Table S6. Comparison of the detection of OTC with other materials.

Material	Method	Linear range (μM)	LOD (μM)	Ref.
Fe_1/SNC	colorimetric	0.3-32 0-0.3	0.126 0.0232	This work
LTN@AuNCs	colorimetric	0.5–15.0	0.3	[34]
CM	Colorimetric	2–100	0.66	[35]
CDsLDHs@MnO2/Fe3O4 magnetic micromotor	Colorimetric	0–100	0.291	[36]
Borophene QDs	Colorimetric	0 – 200	1.10	[37]
N-CDs@Zr hybrid	Colorimetric	0 – 200 200-800	5.04	[38]
CDs	Fluorometric	0 - 40	0.41	[39]
CuNZs	Colorimetric	50–500	0.148	[40]
UIO-66-NH_2	Fluorometric	0-37.5	0.431	[41]
CDs	Fluorescent	10.0–400.0	6.0	[42]

Table S7. Determination of OTC in real samples

Sample	Added (μM)	Detected (μM)	Recovery (%)	RSD (%,n=3)
Medical wastewater (Xiangya Hospital)	0	N	-	-
	0.6	0.626	104.37	3.57
	9	8.351	92.80	1.97
	27	25.108	92.99	2.34
Honey	0	N	-	-
	0.6	0.620	103.33	1.79
	9	9.428	104.76	5.05
	27	24.898	92.21	2.89
Raw milk	0	N	-	-
	0.6	0.571	95.09	6.43
	9	8.550	95.00	4.13
	27	28.442	105.34	5.88

References

[1] Chen, S.; Li, X.; Kao, C.-W.; Luo, T.; Chen, K.; Fu, J.; Ma, C.; Li, H.; Li, M.; Chan, T.-S.; Liu, M. Unveiling the Proton-Feeding Effect in Sulfur-Doped Fe−N−C Single-Atom Catalyst for Enhanced CO_2 Electroreduction. *Angew. Chem. Int. Ed.* **2022***, 61, e202206233*.

[2] Tang, L.-J.; Gao, Z.-W.; Yang, Y.-F.; Liu, Z.-H.; Yang, M.; Song, Z.-Y.; Chen, S.-H.; Huang, X.-J. Sulfur-Engineered Second-Shell in Fe-N_4 Catalysts: Dual Active Sites Harmonized Activity and Stability in Real Water Environment. *Small* **2025***, 21, e06829*

[3] Wang, Y.; Cho, A.; Jia, G.; Cui, X.; Shin, J.; Nam, I.; Noh, K.-J.; Park, B. J.; Huang, R.; Han, J. W. Tuning Local Coordination Environments of Manganese Single-Atom Nanozymes with Multi-Enzyme Properties for Selective Colorimetric Biosensing. *Angew. Chem. Int. Ed.* **2023**, *62*, e202300119.

[4] Xing, Y.; Xiu, J.; Zhou, M.; Xu, T.; Zhang, M.; Li, H.; Li, X.; Du, X.; Ma, T.; Zhang, X. Copper Single-Atom Jellyfish-like Nanomotors for Enhanced Tumor Penetration and Nanocatalytic Therapy. *ACS Nano* **2023**,*17*, 6789–6799.

[5] Li, R.; Jiao, L.; Jia, X.; Yan, L.; Li, X.; Yan, D.; Zhai, Y.; Zhu, C.; Lu, X. Bioinspired FeN5 Sites with Enhanced Peroxidase-like Activity Enable Colorimetric Sensing of Uranyl Ions in Seawater. *Anal. Chem.* **2024**, *96 (7)*, 3124-3130.

[6] Wu, J.; Zhu, X.; Li, Q.; Fu, Q.; Wang, B.; Li, B.; Wang, S.; Chang, Q.; Xiang, H.; Ye, C. Enhancing radiation-resistance and peroxidase-like activity of single-atom copper nanozyme via local coordination manipulation. *Nat. Commun.* **2024**, *15 (1)*, 6174.

[7] Chen, Y.; Wang, P.; Hao, H.; Hong, J.; Li, H.; Ji, S.; Li, A.; Gao, R.; Dong, J.; Han, X. Thermal Atomization of Platinum Nanoparticles into Single Atoms: An Effective Strategy for Engineering High-Performance Nanozymes. *J. Am. Chem. Soc.* **2021**, *143 (44)*, 18643-18651.

[8] Ding, S.; Barr, J. A.; Lyu, Z.; Zhang, F.; Wang, M.; Tieu, P.; Li, X.; Engelhard, M. H.; Feng, Z.; Beckman, S. P.; et al. Effect of Phosphorus Modulation in Iron Single-Atom Catalysts for Peroxidase Mimicking. *Adv. Mater.* **2024**, *36 (10)*, 2209633.

[9] Jiao, L.; Tao, N.; Kang, Y.; Song, W.; Chen, Y.; Zhang, Y.; Xu, W.; Wu, Y.; Gu,

W.; Zheng, L.; Chen, L.; Deng, L.; Zhu, C.; Liu, Y.-N. Biomimetic Fe-Cu Dual-atomic-site Catalysts Enable Efficient H_2O_2 Activation for Tumor Lymphatic Metastasis Inhibition. *Nano Today* **2023**, *50*, 101859.

[10] Jiao, L.; Xu, W.; Zhang, Y.; Wu, Y.; Gu, W.; Ge, X.; Chen, B.; Zhu, C.; Guo, S. Boron-doped Fe-N-C single-atom nanozymes specifically boost peroxidase-like activity. *Nano Today* **2020**, *35*, 100971.

[11] Zhao, Q.; Zhang, M.; Gao, Y.; Dong, H.; Zheng, L.; Zhang, Y.; Ouyang, J.; Na, N. Rearranging Spin Electrons by Axial-Ligand-Induced Orbital Splitting to Regulate Enzymatic Activity of Single-Atom Nanozyme with Destructive d−π Conjugation. *J. Am. Chem. Soc.* **2024**, *146 (21)*, 14875-14888.

[12] Liu, W.; Shi, E.; Wu, H.; Liang, Y.; Chen, M.; Zhang, H.; Zhang, R.; Li, X.; Wang, Y.; Zhang, L. Spatially Axial Boron Coordinated Single-Atom Nanozymes with Boosted Multi-Enzymatic Performances for Periodontitis Treatment. *Adv. Funct. Mater.* **2024**, *34 (39)*, 2403386.

[13] Wei, S.; Ma, W.; Sun, M.; Xiang, P.; Tian, Z.; Mao, L.; Gao, L.; Li, Y. Atom-pair engineering of single-atom nanozyme for boosting peroxidase-like activity. *Nat. Commun.* **2024**, *15 (1)*, 6888.

[14] Ding, S.; Lyu, Z.; Fang, L.; Li, T.; Zhu, W.; Li, S.; Li, X.; Li, J.-C.; Du, D.; Lin, Y. Single-Atomic Site Catalyst with Heme Enzymes-Like Active Sites for Electrochemical Sensing of Hydrogen Peroxide. *Small* **2021**, *17 (25)*, 2100664.

[15] Jiao, L.; Kang, Y.; Chen, Y.; Wu, N.; Wu, Y.; Xu, W.; Wei, X.; Wang, H.; Gu, W.; Zheng, L. Unsymmetrically coordinated single Fe-N3S1 sites mimic the function of peroxidase. *Nano Today* **2021**, *40*, 101261.

[16] Zhu, X.; Wu, J.; Liu, R.; Xiang, H.; Zhang, W.; Chang, Q.; Wang, S.; Jiang, R.; Zhao, F.; Li, Q.; Huang, L.; Yan, L.; Zhao, Y. Engineering Single-Atom Iron Nanozymes with Radiation-Enhanced Self-Cascade Catalysis and Self-Supplied H_2O_2 for Radio-enzymatic Therapy. *ACS Nano* **2022**, *16*, 18849–18862.

[17] Chen, Y.; Wang, P.; Hao, H.; Hong, J.; Li, H.; Ji, S.; Li, A.; Gao, R.; Dong, J.; Han, X. Thermal Atomization of Platinum Nanoparticles into Single Atoms: An Effective Strategy for Engineering High-Performance Nanozymes. *J. Am. Chem. Soc.*

2021, *143 (44)*, 18643-18651.

[18] Zhu, L.; Zhong, H.; Du, D.; Li, T.; Nguyen, H.; Beckman, S. P.; Xu, W.; Li, J.-C.; Cheng, N.; Lin, Y. A peroxidase-like single-atom Fe-N5 active site for effective killing human lung adenocarcinoma cells. *Nano Research* **2023**, *16 (4)*, 5216-5225.

[19] Jiao, L.; Wu, J.; Zhong, H.; Zhang, Y.; Xu, W.; Wu, Y.; Chen, Y.; Yan, H.; Zhang, Q.; Gu, W. Densely Isolated FeN4 Sites for Peroxidase Mimicking. *ACS Catalysis* **2020**, 10 (11), 6422-6429.

[20] Ji, S.; Jiang, B.; Hao, H.; Chen, Y.; Dong, J.; Mao, Y.; Zhang, Z.; Gao, R.; Chen, W.; Zhang, R.; Liang, Q.; Li, H.; Liu, S.; Wang, Y.; Zhang, Q.; Gu, L.; Duan, D.; Liang, M.; Wang, D.; Yan, X.; Li, Y. Matching the Kinetics of Natural Enzymes with a Single-Atom Iron Nanozyme. *Nat. Catal.* **2021**, *4,* 407–417.

[21] Wei, X.; Song, S.; Song, W.; Xu, W.; Jiao, L.; Luo, X.; Wu, N.; Yan, H.; Wang, X.; Gu, W.; Zheng, L.; Zhu, C. Fe_3C-Assisted Single Atomic Fe Sites for Sensitive Electrochemical Biosensing. *Anal. Chem.* **2021**, *93*, 5334–5342.

[22] Xu, W.; Song, W.; Kang, Y.; Jiao, L.; Wu, Y.; Chen, Y.; Cai, X.; Zheng, L.; Gu, W.; Zhu, C. Axial Ligand-Engineered Single-Atom Catalysts with Boosted Enzyme-Like Activity for Sensitive Immunoassay. *Anal. Chem.* **2021**, *93 (37)*, 12758–12766.

[23] Zhu, Y.; Wang, W.; Cheng, J.; Qu, Y.; Dai, Y.; Liu, M.; Yu, J.; Wang, C.; Wang, H.; Wang, S.; Zhao, C.; Wu, Y.; Liu, Y. Stimuli-Responsive Manganese Single-Atom Nanozyme for Tumor Therapy via Integrated Cascade Reactions. *Angew. Chem., Int. Ed.* **2021**, *60 (17)*, 9480–9488.

[24] Zhang, C.; Chen, C.; Zhao, D.; Kang, G.; Liu, F.; Yang, F.; Lu, Y.; Sun, J. Multienzyme Cascades Based on Highly Efficient Metal–Nitrogen–Carbon Nanozymes for Construction of Versatile Bioassays. *Anal. Chem.* **2022**, *94 (8)*, 3485-3493.

[25] Liu, W.; Chen, Q.; Wu, J.; Zhang, F.; Han, L.; Liu, J.; Zhang, H.; Hao, Z.; Shi, E.; Sun, Y. Asymmetric Coordination of Iron Single-Atom Nanozymes with Efficient Self-Cascade Catalysis for Ferroptosis Therapy. *Adv. Funct. Mater.* **2024**, *34 (14)*, 2312308.

[26] Zhao, C.; Xiong, C.; Liu, X.; Qiao, M.; Li, Z.; Yuan, T.; Wang, J.; Qu, Y.; Wang, X.; Zhou, F. Unraveling the enzyme-like activity of heterogeneous single atom catalyst.

Chem. Commun. **2019**, *55 (16)*, 2285-2288.

[27] Wu, Y.; Wu, J.; Jiao, L.; Xu, W.; Wang, H.; Wei, X.; Gu, W.; Ren, G.; Zhang, N.; Zhang, Q.; Huang, L.; Gu, L.; Zhu, C. Cascade Reaction System Integrating Single-Atom Nanozymes with Abundant Cu Sites for Enhanced Biosensing. *Anal. Chem.* **2020**, *92(5)*, 3373–3379.

[28] Xu, W.; Jiao, L.; Yan, H.; Wu, Y.; Chen, L.; Gu, W.; Du, D.; Lin, Y.; Zhu, C. Glucose Oxidase-Integrated Metal–Organic Framework Hybrids as Biomimetic Cascade Nanozymes for Ultrasensitive Glucose Biosensing.*ACS Appl. Mater. Interfaces* **2019**, *11 (25)*, 22096–22101.

[29] Wu, Y.; Wu, J.; Jiao, L.; Xu, W.; Wang, H.; Wei, X.; Gu, W.; Ren, G.; Zhang, N.; Zhang, Q.; et al. Cascade Reaction System Integrating Single-Atom Nanozymes with Abundant Cu Sites for Enhanced Biosensing. *Anal. Chem.* **2020**, *92 (4)*, 3373-3379.

[30] Xu, W.; Jiao, L.; Yan, H.; Wu, Y.; Chen, L.; Gu, W.; Du, D.; Lin, Y.; Zhu, C. Glucose Oxidase-Integrated Metal–Organic Framework Hybrids as Biomimetic Cascade Nanozymes for Ultrasensitive Glucose Biosensing. *ACS Appl. Mater. Interfaces* **2019**, *11 (25)*, 22096–22101.

[31] Xu, B.; Li, S.; Zheng, L.; Liu, Y.; Han, A.; Zhang, J.; Huang, Z.; Xie, H.; Fan, K.; Gao, L. A Bioinspired Five-Coordinated Single-Atom Iron Nanozyme for Tumor Catalytic Therapy. *Adv. Mater.* **2022**, *34 (15)*, 2107088.

[32] Zhao, C.; Xiong, C.; Liu, X.; Qiao, M.; Li, Z.; Yuan, T.; Wang, J.; Qu, Y.; Wang, X.; Zhou, F.; Xu, Q.; Wang, S.; Chen, M.; Wang, W.; Li, Y.; Yao, T.; Wu, Y.; Li, Y. Unraveling the enzyme-like activity of heterogeneous single atom catalyst. *Chem. Commun.* **2019**, *55 (15)*, 2285–2288.

[33] Wu, Y.; Wu, J.; Jiao, L.; Xu, W.; Wang, H.; Wei, X.; Gu, W.; Ren, G.; Zhang, N.; Zhang, Q.; Huang, L.; Gu, L.; Zhu, C. Cascade Reaction System Integrating Single-Atom Nanozymes with Abundant Cu Sites for Enhanced Biosensing. *Anal. Chem.* **2020**, *92(5)*, 3373–3379.

[34] Zhang, X.; Qiao, J.; Liu, W.; Qi, L. Boosting the peroxidase-like activity of gold nanoclusters for the colorimetric detection of oxytetracycline in rat serum. *Analyst* **2021**, *146(16)*, 5061–5066.

[35] Zhang, T.; Zhang, Z.; Sun, S.; Qu, X.; Qiu, Y.; Kai, T.; Wu, P.; Ding, P. Multi-functional copper-manganese Nanozyme-Driven integrated platform for Fluorescence/Colorimetric Dual-Mode Detection, catalytic degradation of oxytetracycline and antibacterial disinfection. *Sep. Purif. Technol.* **2025**, *374*, 133751.

[36] Liu, C.; Li, J.; Zuo, M.; Ng, D. H. L.; Yang, X.; Gao, S.; Lan, Z. Synthesis of carbon dot LDHs@MnO_2 tubular magnetic micromotors for detection and degradation of oxytetracycline. *Sep. Purif. Technol.* **2024**, *340*, 126650.

[37] Gogoi, D.; Hazarika, C.; Neog, G.; Mridha, P.; Bora, H. K.; Das, M. R.; Szunerits, S.; Boukherroub, R. Borophene Quantum Dots as Novel Peroxidase-Mimicking Nanozyme: A Dual-Mode Assay for the Detection of Oxytetracycline and Tetracycline Antibiotics. *ACS Appl. Mater. Interfaces* **2024**, *16(11)*, 14645–14660.

[38] Li, Y.; Kuang, Z.; Li, X.; He, L.; Yang, Z.; Yang, J.; Wang, X. Photoresponsive N-CDs@Zr luminescent nanozyme for dual-mode optical detection of oxytetracycline. *Microchem. J.* **2025**, *212,* 113500.

[39] Fu, Y.; Huang, L.; Zhao, S.; Xing, X.; Lan, M.; Song, X. A Carbon Dot-Based Fluorometric Probe for Oxytetracycline Detection Utilizing a Förster Resonance Energy Transfer Mechanism. *Spectrochim. Acta, Part A* **2020**, *246*, 118947.

[40] Wu, C.; Li, J.; Song, J.; Guo, H.; Bai, S.; Lu, C.; Peng, H.; Wang, X. Novel Colorimetric Detection of Oxytetracycline in Foods by Copper Nanozyme. *Food Chem.* **2024**, *430*, 137040.

[41] Wang, X.; Wang, X. UIO-66-NH_2 Based Fluorescent Sensing for Detection of Tetracyclines in Milk. *RSC Adv.* **2022**, *12 (36)*, 23427–23436.

[42] Yan, Y.; Liu, J. H.; Li, R. S.; Li, Y. F.; Huang, C. Z.; Zhen, S. J. Carbon Dots Synthesized at Room Temperature for Detection of Tetracycline Hydrochloride. *Anal. Chim. Acta* **2019**, *1063*, 144–151.